

Carbon emissions from the edge of the Greenland Ice sheet reveal subglacial processes of methane and carbon dioxide turnover

Jesper Riis Christiansen¹, Thomas Röckmann², Maria Elena Popa², Celia Julia Sapart³, and Christian Juncher Jørgensen⁴

¹University of Copenhagen

²Utrecht University

³Laboratoire de glaciologie

⁴Aarhus University

November 23, 2022

Abstract

Emission of methane (CH₄) and CO₂. *In situ* mole fractions of CH₄ and CO₂ were measured in the subglacial air at a subglacial river outlet where emissions of CH₄ and CO₂ had been identified. Water samples were analysed for dissolved CH₄ and CO₂ concentrations. CH₄ and CO₂ in gas and water samples were analyzed for their isotopic composition of ¹³C and ²H. Close correlation between gaseous and dissolved CH₄ and CO₂, respectively, show degassing of CH₄ and CO₂ from the subglacial meltwater. The diurnal variability of *in situ* mole fractions of CH₄ and CO₂ in subglacial air was related to meltwater runoff. Maximum *in situ* mole fractions decreased after the peak of the melt season, but estimated net emissions increased because the size of the subglacial river outlet increased. The isotopic signature of CH₄ in the subglacial air, estimated with a Keeling plot, indicated that subglacial CH₄ likely originated from acetoclastic methanogenesis. Isotopic signatures of gaseous CO₂ indicate that both microbial oxidation of CH₄ in the subglacial system and remineralization of carbon in subglacial sediments contribute to subglacial CO₂.

1 **Carbon emissions from the edge of the Greenland Ice sheet reveal subglacial**
2 **processes of methane and carbon dioxide turnover**

3 Jesper R. Christiansen^{1*}, Thomas Röckmann², Maria E. Popa², Celia J. Sapart^{3†}, Christian J. Jørgensen⁴

4 ¹Department of Geoscience and Natural Resource Management, University of Copenhagen,
5 Denmark.

6 ²Institute for Marine and Atmospheric research Utrecht (IMAU), Utrecht University,
7 Netherlands.

8 ³Laboratoire de Glaciologie, Libre Université de Bruxelles, Belgium.

9 ⁴Arctic Environment, Department of Bioscience, Aarhus University, Denmark

10 Correspondance to: Jesper R. Christiansen (jrc@ign.ku.dk)

11 † Current affiliation: CO₂ Value Europe, Belgium.

12 **Key Points:**

- 13 • Highly elevated CH₄ (up to 250 ppm) and CO₂ (up to 640 ppm) in subglacial air indicate
14 high emissions of both gases from below the ice sheet
- 15 • Gaseous CH₄ and CO₂ originate from gases dissolved in the meltwater.
- 16 • The isotopic signature and composition of subglacial CH₄ in gas and meltwater show that
17 it originates from microbial acetate fermentation
- 18 • Isotopic signatures of subglacial gCO₂ indicate that both methane oxidation and
19 remineralisation are likely subglacial sources of CO₂

20 Abstract

21 Emission of methane (CH₄) and carbon dioxide (CO₂) from the subglacial environment under
22 Greenland Ice Sheet (GrIS) was only recently discovered. The understanding of mechanisms and
23 magnitudes of emissions, and the origin of the gases, is extremely sparse. This study reports the
24 magnitude and temporal variations in net emissions at the onset, near maximum and at the end of
25 the melt season in 2018 and 2019 and investigates the possible origin of the subglacial CH₄ and
26 CO₂. *In situ* mole fractions of CH₄ and CO₂ were measured in the subglacial air at a subglacial
27 river outlet where emissions of CH₄ and CO₂ had been identified. Water samples were analysed
28 for dissolved CH₄ and CO₂ concentrations. CH₄ and CO₂ in gas and water samples were
29 analyzed for their isotopic composition of ¹³C and ²H. Close correlation between gaseous and
30 dissolved CH₄ and CO₂, respectively, show degassing of CH₄ and CO₂ from the subglacial
31 meltwater. The diurnal variability of *in situ* mole fractions of CH₄ and CO₂ in subglacial air was
32 related to meltwater runoff. Maximum *in situ* mole fractions decreased after the peak of the melt
33 season, but estimated net emissions increased because the size of the subglacial river outlet
34 increased. The isotopic signature of CH₄ in the subglacial air, estimated with a Keeling plot,
35 indicated that subglacial CH₄ likely originated from acetoclastic methanogenesis. Isotopic
36 signatures of gaseous CO₂ indicate that both microbial oxidation of CH₄ in the subglacial system
37 and remineralization of carbon in subglacial sediments contribute to subglacial CO₂.

38 Plain Language Summary

39 Wetlands and thawing permafrost are considered to be the primary sources of natural
40 methane and carbon dioxide emissions in the Arctic. However, new discoveries show that these
41 gases are also emitted in large quantities from the meltwater coming from under the Greenland
42 Ice sheet. So far, subglacial gas emissions have only been investigated at two sites in Greenland
43 and it is not known how much gas is released, where it comes from and how sensitive the
44 emissions are to future climate change. The aim of our research is to investigate how much is
45 emitted to the atmosphere and what the likely origin of these gases are. Our field measurements
46 show that the levels of methane and carbon dioxide in the glacial outlet cavity are up 100 times
47 higher than the background levels of methane in the atmosphere. Our results show that these
48 gases originate from biological processes under the ice, and that the release rate is controlled by
49 the melting of the glacier. Our study reveals new insight in to this unknown Arctic source of

50 greenhouse gases which will help us to understand its broader relevance for the atmospheric
51 composition and its feedback to climate change.

52 **1 Introduction**

53 Ice sheets and glaciers separate large parts of the earth's rocky surface and sediment
54 deposits from the atmosphere. Until recently it was perceived that glaciated areas had no
55 significant impact on the global carbon cycle and that only little carbon was exchanged across
56 this separating layer. Recent research results have challenged this view by showing that large
57 exports of both methane (CH₄) and carbon dioxide (CO₂) can occur from subglacial
58 environments (Burns et al., 2018; Christiansen & Jørgensen, 2018; Lamarche-Gagnon et al.,
59 2019; Pain et al., 2020). Estimates show that the subglacial CH₄ export in melt water from the
60 Leverett glacier draining the Greenland Ice sheet (GrIS) can rival those of major world rivers
61 (Lamarche-Gagnon et al., 2019). This points to an overlooked, and likely significant, source of
62 CH₄ and CO₂ emissions to the atmosphere, which is a natural constituent of the global carbon
63 cycle that may be affected by global climate change.

64 Elevated concentrations and biological production of CH₄ in subglacial waters and
65 sediments have been found under glaciers and ice sheets across Canada (Hamilton et al., 2013),
66 Antarctica (Michaud et al., 2017; Stibal et al., 2012), West Greenland (Dieser et al., 2014),
67 Iceland (Burns et al., 2018) and at the center of the GrIS (Christner et al., 2012; Souchez et al.,
68 1995). Once formed under the ice, the CH₄ may either be stored as dissolved gas in the basal
69 meltwater or accumulate as hydrates under high pressure (i.e. solid CH₄ bound in a crystal
70 structure with water molecules) (Wadham et al., 2012) both of which eventually will be exported
71 to the proglacial zone via meltwater rivers and emitted to the atmosphere. Microbial potential to
72 oxidize subglacial biological CH₄ to CO₂ has also been documented in sediment and water
73 samples from below the GrIS and Antarctica (Dieser et al., 2014; Michaud et al., 2017).
74 These findings point to the potential occurrence of widespread subglacial biological processes
75 responsible for production of CH₄ and CO₂ that can be emitted to the atmosphere. Organic
76 carbon reserves in overridden paleosoils (Kohler et al., 2017) or marine sediments (Wadham et
77 al., 2012) below ice sheets worldwide could surpass the amount stored in non-glaciated
78 permafrost areas (Wadham et al., 2019). If this carbon is or becomes available to microbial
79 degradation into CH₄ and CO₂ in the subglacial environment it potentially represents a large, but
80 little known emission magnitude of these gases to the atmosphere.

81 The very limited empirical evidence from field studies on subglacial CH₄ and CO₂
82 turnover processes and emissions (Burns et al., 2018; Christiansen & Jørgensen, 2018;
83 Lamarche-Gagnon et al., 2019) is insufficient for understanding of the importance of subglacial
84 carbon conversion for the atmospheric CO₂ and CH₄ composition and whether it can be regarded
85 as potential climate amplifier (Wadham et al., 2008, 2019). In this paper we present new findings
86 from field work carried out in the summers of 2018 and 2019 adding to fill our knowledge gap
87 on subglacial carbon emission rates and turnover processes. We performed *in situ* high frequency
88 measurements of the mole fractions of CH₄ and CO₂ in the subglacial air inside the air-filled ice
89 cavities found at the ice edge, and collected discrete gas and water samples for analyses of the
90 isotopic composition of CH₄ and CO₂. The aims were to 1) measure the magnitude of subglacial
91 carbon fluxes to the atmosphere at the onset, near maximum and late stages of the melt season,
92 2) to study the diurnal and seasonal temporal dynamics of subglacial CO₂ and CH₄ emissions and
93 their relation with glacial hydrology, and 3) to investigate the potential sources of subglacial CH₄
94 and CO₂.

95 **2 Materials and Methods**

96 **2.1 Site description**

97 The study site is located at an elevation of 450 m above sea level at a lateral subglacial
98 meltwater outlet on the southern flank at the terminus of the Isunnguata Sermia Glacier at the
99 western margin of the GrIS (67°09'16.40''N 50°04'08.48''W).

100 The area in front of the meltwater outlet consists of abraded granodioritic gneiss bedrock
101 with large boulders and patches of gravel, sand and silt deposited by meltwater. The glacier front
102 contained highly irregular cracks and air-filled cavities, which changed over the season as the ice
103 melted and deformed (Figure 1).

104 The landscape in the Kangerlussuaq area is typical of west Greenland, where numerous,
105 narrow and up to 600 meter deep valleys are oriented in a East - West direction. These valleys
106 extend below the ice sheet, and subglacial valleys can in places reach depths of hundreds of
107 meters below sea level. Deglaciation and re-advance of the GrIS in this region during the
108 Holocene has resulted in buried subglacial carbon rich sediments that were once exposed
109 (Kellerman et al., 2020; Kohler et al., 2017). In the proglacial zone of the study area continuous
110 permafrost extends at places up to 350 meters below the surface (Drake et al., 2017), but the

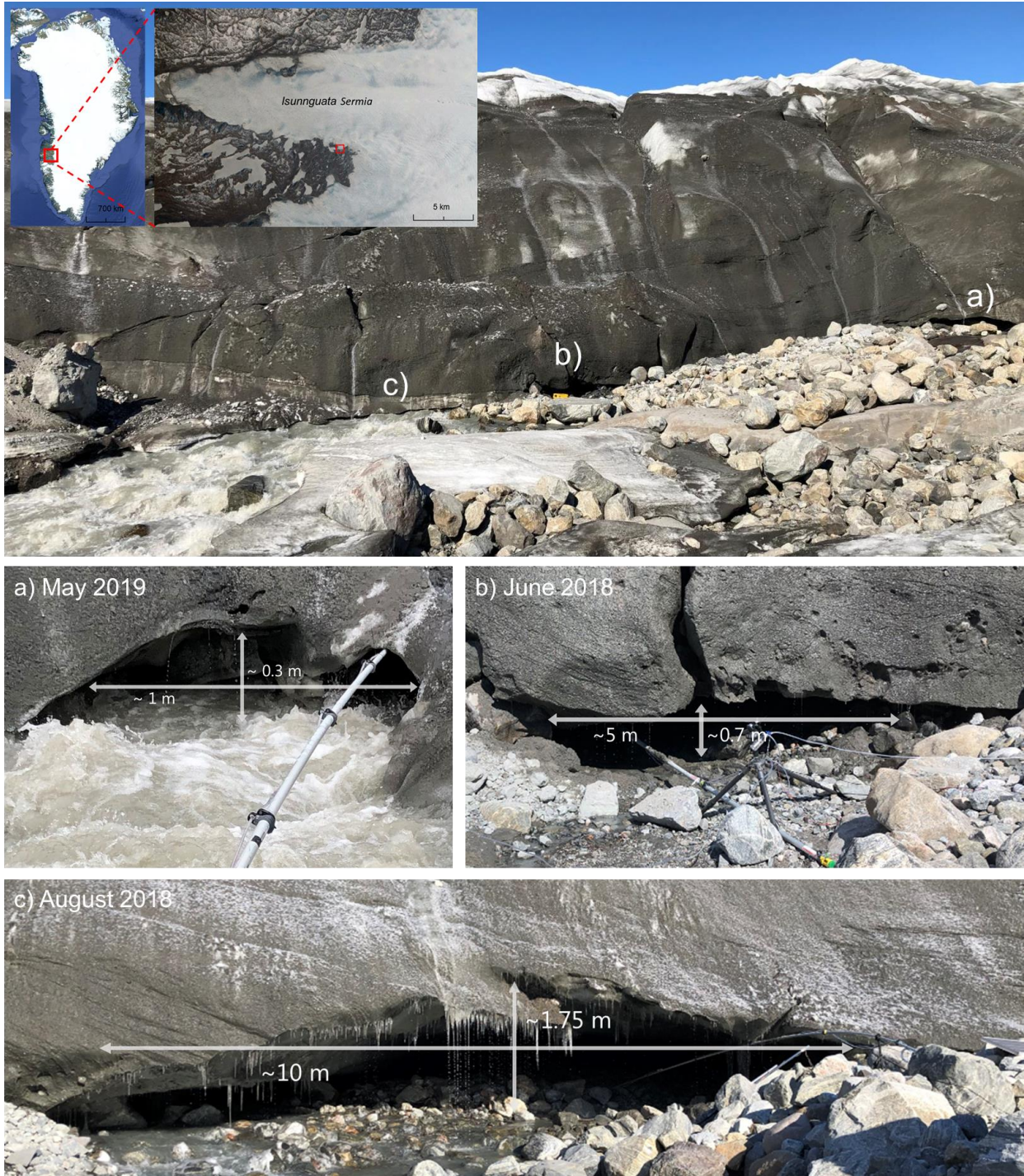
111 Isunnguata glacier and GrIS in this area is warm based with an annual ice flow of 150-200
112 meters and surface meltwater reaching the base of the glacier (Graly et al., 2014).

113 We sampled melt water and gas at a lateral subglacial outlet to the Isunnguata Sermia
114 glacier draining the GrIS in West Greenland (Figure 1 top panel). The sampling was done during
115 three campaigns covering the periods May 3rd to 6th 2019, June 18th to 28th and August 16th to
116 24th 2018, during which the cross sectional area of the subglacial outlet changed size and
117 position along the ice edge (Figure 1a-c). These periods are assumed to represent the early,
118 middle and late stages of a typical melt season.

119 2.2 Measurements of subglacial air velocity, temperature, humidity, atmospheric pressure and
120 water level

121 At the end of an aluminium pole that extended under the ice for retrieval of unmixed
122 subglacial air we attached instrumentation to measure subglacial air velocity (hot-wire
123 anemometer, model 313-T-DCI-F900-L-O, Onset Computer Cooperation, USA), temperature
124 and humidity (model 313-S-THB-M008, Onset Computer Cooperation, USA). The anemometer
125 was positioned so it measured the wind movement perpendicular to the cross section.
126 Atmospheric pressure was measured outside the cave (model 313-S-BPB-CM50, Onset
127 Computer Cooperation, USA). The data were recorded on a HOBO datalogger (model U30-
128 NRC-VIA-05-S100-000, Onset Computer Cooperation, USA) at 10 second intervals. These
129 measurements were conducted during the June and August campaigns only. We were only able
130 to measure the air velocity for a short period in June as the sensor was damaged by water spray
131 in the ice cave.

132 During the August 2018 campaign, we also installed an underwater pressure transducer
133 (Onset Computer Corporation, USA) in the outlet stream to estimate the temporal variability of
134 the water level. Air pressure from the meteorological station was used as the atmospheric
135 reference needed to calculate the water level above the pressure transducer. The water level was
136 assumed as a proxy for melt water runoff, but the discharge volume was not estimated.



137

138 **Figure 1** Top panel: Map of West Greenland and Isunnguata glacier with study site indicated at red squares (top left inset) and
 139 an overview of the study site at the ice front in June 2018. Letters (a, b, c) indicate location of measurement of mole fractions of
 140 CH_4 and CO_2 in subglacial air and sampling of melt water at three different stages during the melt season. a) May 2019
 141 represents the early stage meltwater discharge where the meltwater openings are small and mostly filled with water. b) June
 142 2018 represents a progressive stage of opening where multiple cracks and caves are air filled after the meltwater has carved out
 143 channels in the ice. c) August 2018 represents the mature stage of evolution of the meltwater channel, where the volume of the
 144 outlet is at its maximum and most of it is air filled due to decreasing meltwater volumes.

145

146 2.3 Measurements of gaseous subglacial CH₄ and CO₂ mole fractions and flux calculation

147 Dry mole fractions of CH₄ and CO₂ in the subglacial air were measured with a portable
 148 CH₄/CO₂/H₂O analyzer (Ultraportable Greenhouse Gas Analyzer (UGGA), ABB Los Gatos
 149 Research, USA) powered by a 12 V 100 Ah LiFePO₄ battery. Due to shifting positions and
 150 geometries of the subglacial cave, the gas sampling setup with the UGGA was not identical
 151 during all campaigns, but generally followed the same procedure (Figure 1a-c). The cross
 152 sectional areas of the outlet during the three campaigns were estimated based on field
 153 observations of the dimensions (height and width) of the opening (Figure 1a-c). Gas
 154 measurements were performed by attaching a tube to a 9 m aluminium pole and sampling the air
 155 inside the subglacial cavities (Figure 1a-c). A water trap fixed to the end of the aluminium pole
 156 ensured a liquid free air stream to the gas analyzer.

157 The net CH₄ and CO₂ emission (g CH₄ s⁻¹ or g CO₂ s⁻¹) across the entire cross sectional
 158 area from the subglacial cave to the atmosphere was calculated as a mass flow of air through the
 159 estimated cross section area according to equation 1:

$$160 F_{CO_2/CH_4} = C * \bar{v} * A * \frac{273.15}{(M_v * T_a)} * M * 10^{-6} \quad (\text{equation 1})$$

161 Where C is the measured 0.1 Hz dry mole fraction ($\mu\text{mol mol}^{-1}$) of CO₂ or CH₄, \bar{v} is the wind
 162 speed (m s^{-1}) measured every 10 seconds perpendicular to the cross section, A is the cross
 163 sectional area at the given measurement period (m^2), M_v is the molar volume ($\text{m}^3 \text{mol}^{-1}$), T_a is the
 164 air temperature ($^{\circ}\text{K}$) measured in the cavity, M is the molar mass of CO₂ or CH₄ (g mol^{-1}), the
 165 constant 10^{-6} converts the flux from μg to g CO₂/CH₄. The cross sectional area was estimated
 166 based on the width and height measured in the field (Figure 1a-c). To estimate and compare the
 167 net CH₄ and CO₂ emission between campaigns we assumed that the average wind speed
 168 ($0.8 \pm 0.28 \text{ m s}^{-1}$) measured in June 2018 and air temperature (0.2°C) in the cavity was similar
 169 between and constant during the three measurement periods. The average hourly net emission for
 170 each measurement period was then calculated as the sum of 0.1 Hz emissions over the
 171 measurement period divided by length in hours of the measurement periods. This approach
 172 provide at best a rough and uncertain estimate, referred to as “plausible range”, and was
 173 calculated as the emission for the minimum wind speed at the minimum cross section area and
 174 maximum wind speed for the maximum cross section area. The impact of short term influx of

175 CH₄ and CO₂ from the atmosphere to the cave, due to turbulent mixing, was accounted for by
176 averaging the 0.1 Hz effluxes over the measurement period.

177 2.4 Collection of discrete water and gas samples

178 Water and gas samples were taken at three different locations after the subglacial water
179 and air had mixed to different degrees with the ambient environment. For the air samples, the
180 simultaneous variations in mole fraction and isotopic composition were used to determine the
181 isotopic composition of the source ($\delta^{13}\text{C-CH}_4$, $\delta^2\text{H-CH}_4$ and $\delta^{13}\text{C-CO}_2$) of the subglacial CH₄ and
182 CO₂ using the Keeling plot approach. This is a widely used method to determine the isotope
183 composition of unknown sources of CO₂ or CH₄ in situations where CH₄ or CO₂ from a source
184 (in our case the subglacial environment) is added to a constant background (atmosphere) (Pataki
185 et al., 2003).

186 Water and gas were sampled twice per day, in the morning and evening, assumed to
187 represent low and high water flow derived from the water level measurements. In 2018, samples
188 were gathered during the periods 22nd – 26th June and 19th – 22nd August.

189 Air samples were collected in 2L gas tight aluminium foil bags (SupelTM-Inert Multi-
190 Layer Foil, Sigma-Aldrich, USA) which were filled by a small diaphragm pump. We sampled
191 gas from three locations (Figure 1a-c); inside the ice cave, representing the least mixed
192 subglacial air we could possibly sample (minimal mixing with atmosphere), right outside the ice
193 cave (subglacial air mixed with atmospheric air) and 2 km from the ice edge (background
194 atmosphere, no subglacial air signal).

195 For practical reasons the water was sampled at slightly different positions than the gas.
196 Thus, the first water sample representing the subglacial water was sampled right where the
197 meltwater exists the ice (PW1), the second sample (PW2) 200 meter downstream and the third
198 sample was taken at the same position as the third gas sample, 2 km away from the ice edge
199 (PW3). Unfiltered water was sampled in 120 mL glass bottles with butyl rubber septa and
200 tightened with aluminium screw caps. The bottles were rinsed three times with melt water and
201 filled under water ensuring that no bubbles were included. Immediately after sampling, 12 μL
202 saturated HgCl₂ solution was added to the bottles to exclude further biological activity (Magen et
203 al., 2014). Water was sampled in duplicates, one sample for measurement of dissolved CH₄ and
204 another for measurement of CH₄ isotopic composition.

205 Gas and water samples were stored cold and dark until analysis, except during transport
 206 from Greenland to Denmark where samples were transported in the cargo hold of the airplane.
 207 Transport resulted in loss of three gas samples, but water samples remained intact. Upon arrival
 208 in Denmark the gas bags were immediately sent to Utrecht over land and transferred to glass
 209 bottles for longer term storage until isotopic analyses were possible. The total time from
 210 sampling to extraction was up to 14 days.

211 2.5 Dissolved CH₄ concentrations

212 The dissolved CH₄ was extracted using headspace mixing and the concentration was
 213 calculated according to the method outlined in Magen et al. (2014). Shortly, 10 mL of water
 214 (V_{HS}) was replaced with CH₄ free N₂ gas and the headspace was afterwards pressurized to 2
 215 atmosphere (P_{HS}), by adding another 10 mL N₂ amounting to 20 mL of gas in the headspace
 216 (V_{gas}). The sample was then thoroughly stirred on a shaking table with 150 RPM for three
 217 minutes. A 5 mL gas sample was retrieved by syringe from the headspace and transferred to an
 218 evacuated 3 mL exetainer with a butyl rubber screw cap (Labco, UK). The pressurization of the
 219 exetainer was done to facilitate subsequent gas chromatography analysis. The CH₄ mole fraction
 220 in the headspace (CH_{4,mf}) of extracted gas samples was determined on a gas chromatograph
 221 equipped with an FID detector. CH₄ was separated on a HayeSep Q column heated to 60°C, with
 222 pure N₂ 5.0 as carrier gas. Using a five-point calibration curve the headspace CH₄ mole fraction
 223 in ppm was determined. The total dissolved CH₄ was calculated as the sum of the headspace CH₄
 224 and CH₄ still dissolved in the water after shaking (Magen et al. 2014). The ideal gas law was
 225 used (laboratory temperature at extraction was 23°C) to convert the headspace concentration to
 226 gas amount (mole) (equation 2). The dissolved CH₄ in the remaining 110 mL water was
 227 calculated by multiplying the Bunsen coefficient for 0°C (water temperature at sampling) at zero
 228 salinity (assumed as we have no data) with the amount of headspace CH₄ to calculate the
 229 remaining dissolved CH₄ in water (Yamamoto et al., 1976), accounting for the ratio of water and
 230 gas volume (Magen et al., 2014) (equation 3).

$$231 \quad CH_{4,HS} = CH_{4,mf} * V_{HS} * \frac{P_{HS}}{R * T_{HS}} [\mu mol L^{-1}] \quad (\text{equation 2})$$

$$232 \quad CH_{4,water} = \beta * \frac{CH_{4,conc} * V_{gas} * \frac{V_{water}}{V_{HS}}}{R * T_{water}} [\mu mol L^{-1}] \quad (\text{equation 3})$$

233 Where $\text{CH}_{4,\text{conc}}$ is the headspace CH_4 mole fraction in ppm, V_{HS} is the headspace volume in L,
234 P_{HS} is the headspace pressure in atm, R is the gas constant ($\text{atm L K}^{-1} \text{mol}^{-1}$), T_{HS} is the
235 headspace temperature in °K, β is the Bunsen coefficient, V_{gas} is the total volume of gas in
236 headspace in L, V_{water} is the water volume after replacement in L, T_{water} is the water temperature
237 (similar to T_{HS}).

238 2.6 Dissolved CO_2 concentrations

239 Dissolved CO_2 in meltwater was measured *in situ* using an eosGP2 probe (Eosense Inc.,
240 Canada) connected to a Campbell CR1000 datalogger (Campbell Scientific Inc., USA) during
241 the June 2018 campaign. The sampling interval was 10 seconds and dissolved CO_2
242 concentrations given in ppm. A custom calibration for measurements at CO_2 concentrations close
243 to the atmospheric equilibrium had been done prior to the field work by Eosense. Before each
244 deployment, we let the eosGP2 probe equilibrate with the atmospheric background CO_2
245 concentration for approximately one hour to monitor possible drift and/or sensitivity of the
246 response of the CO_2 signal when switching the probe between the aqueous and gaseous phases.
247 At deployment the eosGP2 probes were fixed in place and the diffusion membrane initially
248 placed 15 cm below the surface of the meltwater at low flow conditions.

249 2.7 Isotopic analyses of gas and water samples

250 The isotopic composition of CH_4 ($\delta^{13}\text{C}\text{-CH}_4$, $\delta^2\text{H}\text{-CH}_4$) was measured using continuous-
251 flow isotope ratio mass spectrometry (CF-IRMS) on a ThermoFinnigan Delta^{plus} XL isotope ratio
252 mass spectrometer. The air samples were injected via a mass flow controller into the sample loop
253 of the extraction system and further processed and analyzed as described in Röckmann et al.
254 (2016). The CH_4 in the water samples was extracted with a headspace mixing method and further
255 analyzed on the same analytical system, as described in Jacques et al. (2020). Further
256 information on the data processing is available in Brass and Röckmann (2010) and Sapart et al.
257 (2011). Specifically, the CH_4 isotopic data were corrected to account for system variability and
258 non-linearity effects and reported in ‰ vs VPDB for $\delta^{13}\text{C}$ values and ‰ vs VSMOW for $\delta^2\text{H}$
259 values. The measurement reproducibility was calculated from the standard deviation of reference
260 air injections.

261 The isotopic composition of CO_2 ($\delta^{13}\text{C}$ and $\delta^{18}\text{O}$) was analyzed with the CF-IRMS

262 system described in Naus et al. (2018) and Pathirana et al. (2015). This system is primarily
263 meant for CO isotopes, but can also analyze CO₂ isotopes in small samples (~ 2 ml air at normal
264 atmospheric mole fractions). In short, the CO₂ is cryogenically separated from the air, further
265 purified chromatographically, and then injected into the IRMS via an open split inlet. The results
266 are related to the VPDB and VSMOW scales via a reference air cylinder with known isotopic
267 composition. The typical precision, estimated as repeatability of multiple measurements of a
268 constant gas (Target cylinder), is about 3 ppm for the CO₂ mole fractions, and 0.05 ‰ and 0.14
269 ‰ for $\delta^{13}\text{C}$ and $\delta^{18}\text{O}$ respectively.

270 **3. Results and discussion**

271 3.1 Subglacial CH₄ and CO₂ mole fractions and concentrations in air and meltwater

272 Figure 2 shows measured mole fractions of gaseous CH₄ (gCH₄) and CO₂ (gCO₂) (Figure
273 2a-c) and concentrations of dissolved CH₄ (dCH₄) (Figure 2d-f) for the three campaigns. During
274 all campaigns the gCH₄ and gCO₂ mole fractions measured at the outlet were continuously and
275 significantly elevated compared to the ambient mole fractions of these gases (Figure 2a-c). Also
276 in the water, dCH₄ concentrations are strongly elevated compared to the saturation concentration
277 of CH₄ (0.02 $\mu\text{mol L}^{-1}$) in contact with ambient air (Figure 2d-f). Collectively, this clearly
278 demonstrates that a source for these gases exists below the ice sheet.

279 Concentrations of dCH₄ were highest close to the outlet and decreased strongly with
280 distance from the outlet. Degassing is assumed to be the main loss process for dCH₄ from the
281 meltwater between the sampling points PW1 and PW3 (Christiansen & Jørgensen, 2018).
282 Oxidation of dCH₄ to CO₂ can contribute as well, but oxidation rates measured previously are
283 low (Dieser et al., 2014), indicating that it cannot be the main cause for the observed decrease
284 here. The dCH₄ at PW3 occasionally is lower than the atmospheric equilibrium during the June
285 and August 2018 campaigns, but it is not possible to determine if it is attributed to the inherent
286 uncertainty of dCH₄ determination or in-stream oxidation of CH₄ (Figure 2D-E).

287 In the June and August campaigns both CH₄ and CO₂ showed diurnal variability with
288 some inconsistency between the gases, which indicate that several factors contribute to this
289 observed variability (Figure 2A-C).

290 In June 2018, the temporal behavior of gCH_4 and gCO_2 were related to variations in melt
291 water and maximum mole fractions of both gases generally occurred at low flow conditions. A
292 possible explanation is that during the period of low water flow less surface water purges the
293 subglacial environment, and the dCH_4 and dCO_2 , which presumably, are released at a constant
294 rate from the source under the ice, accumulates in this smaller volume of water, increasing the
295 concentrations. Degassing subsequently enriches the subglacial air with CH_4 and CO_2 .
296 Additionally, the increase of melting during the day will dilute the CH_4 and CO_2 bearing
297 subglacial meltwater resulting in lower degassing and hence lower mole fractions in the
298 subglacial air at high water flow. The control of degassing on gCH_4 and gCO_2 mole fractions is
299 supported by simultaneous measurements of gCO_2 and dCO_2 in the June campaign (Figure S2A)
300 and water level for a single diurnal cycle. These measurements showed identical temporal
301 variability of dCO_2 and gCO_2 , with maximum dCO_2 and gCO_2 occurring at low flow and higher
302 dCO_2 concentrations relative to gCO_2 (Figure S2) strongly suggesting that the meltwater is the
303 source of gCO_2 .

304 In the August 2018 campaign the diurnal pattern of gCH_4 and partly that of gCO_2 were
305 slightly different than observed in June 2018 and anti-correlated to the flow variations observed
306 in the melt water river in August (Figure S1), with maximum gCH_4 and gCO_2 arriving at the
307 outlet on average 6 hours after minimum flow (Figure S1). At this waning stage of the melt
308 season the internal drainage system has reached its maximum volume, which may not be entirely
309 water filled because of lower melt rates. This could potentially leave air filled subglacial caves
310 where CH_4 and CO_2 can accumulate during low flux and the release to the atmosphere occurs
311 more slowly due to slower transport of the subglacial air compared to the melt water. In the early
312 stage of the melt season, where the drainage system volume is smaller and mostly filled with
313 water, most degassing more likely occurs closer to the outlet. In the May 2019 campaign, where
314 no visible caves had developed at the edge (representing the early melt season) diurnal variability
315 was difficult to discern.

316

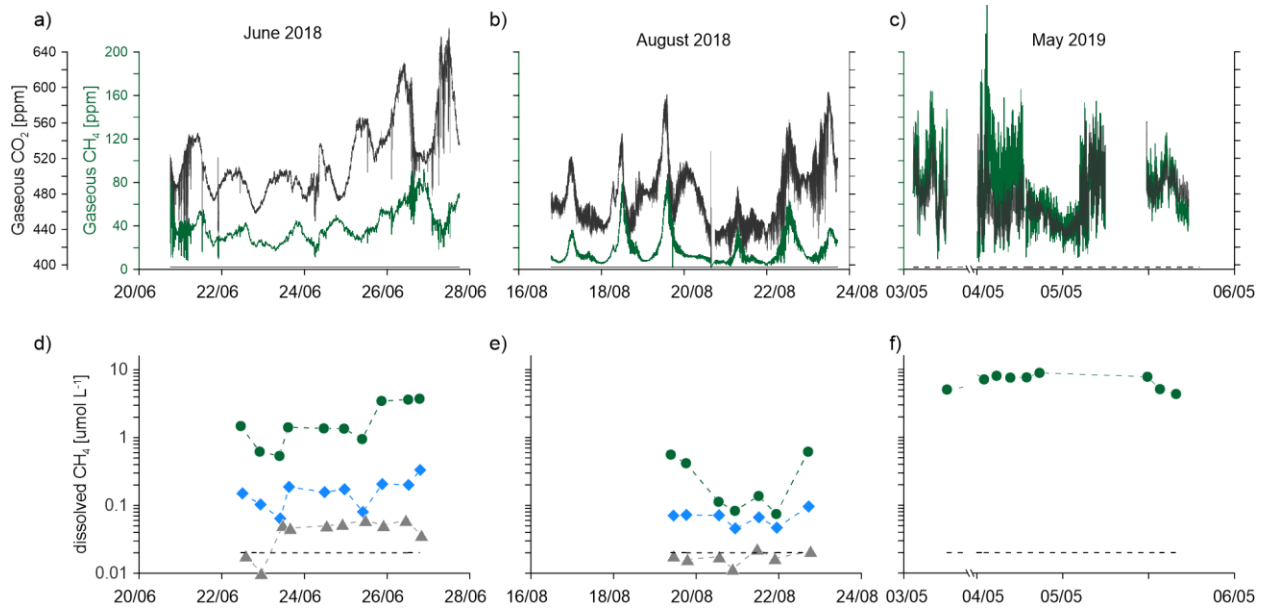
317

318

319 *Table 1* Average, minimum and maximum gaseous subglacial CH_4 and CO_2 mixing ratios in May 2019, June 2018 and August
 320 2018 campaigns. *The enrichment factor ($x_{Atmosphere}$) relative to the atmospheric background for CH_4 and CO_2 is based on in
 321 situ measurements of the atmospheric mole fractions of $CH_4 = 2$ ppm and $CO_2 = 400$ ppm.

	CH_4 mole fraction [ppm]				CO_2 mole fraction [ppm]			
	Average	Min	Max	$x_{Atmosphere}^*$	Average	Min	Max	$x_{Atmosphere}^*$
May 2019	70.8	6.67	243	35.4	476	425	580	1.2
June 2018	40.4	8.06	92.1	20.2	521	426	667	1.3
August 2018	18.6	3.68	87.5	9.3	479	397	596	1.2

322



323

324 **Figure 2** Upper panels: Time series of subglacial gaseous CH_4 (green) and CO_2 (grey) mole fractions in a) June 2018, b) August
 325 2018 and c) May 2019. Black dashed line indicates the atmospheric mole fractions of CH_4 (2 ppm) and CO_2 (400 ppm) measured
 326 on site. Lower panels: Dissolved CH_4 concentrations at three distances (● PW1: 0 m from outlet; ◆ PW2: 200 m from the
 327 outlet; ▲ PW3: 2000 meter from the outlet) for d) June 2018, e) August 2018 and f) May 2019. Black dashed line indicates the
 328 estimated dissolved concentration of CH_4 at atmospheric equilibrium ($0.02 \mu mol L^{-1}$). For interpretation of colours the reader is
 329 referred to the online publication.

330 Both the level and the temporal variability of gCH_4 mole fractions were different between
 331 the seasons, with the highest average and maximum measured in May 2019, followed by June
 332 2018 and the lowest average mole fractions in August 2018 (Table 1, Figure 2a-c). The average
 333 enrichment factor (gCH_4 /atmospheric CH_4) decreased from May to August from 35 to 9 (Table
 334 1). For gCO_2 there was less difference between the seasons and the average enrichment factor
 335 was 1.2 – 1.3 (Table 1). Taking the development of the cross-section area (Christiansen &

336 Jørgensen, 2018) during field campaigns into account and using the average wind speed \pm one
 337 standard deviation, it was estimated that the range of hourly CH_4 and CO_2 fluxes increased from
 338 May to August (Table 2) despite lower average mole fractions. We note that our total estimate
 339 uses several approximations. Notably, we assume constant wind speed of subglacial air and air
 340 temperature across the seasonal variation in cross section of the ice cave. It was previously
 341 estimated that the subglacial air velocity could reach up to 2 m s^{-1} (Christiansen & Jørgensen,
 342 2018) and in this study we observed fluctuations of the wind speed in this range from 0.1 to 2.5
 343 m s^{-1} (Figure S3) with an average speed of 0.8 m s^{-1} and a standard deviation of 0.28 m s^{-1} .
 344 Improving the measurement of the subglacial air velocity is key for more accurate quantification
 345 of gaseous flux estimates in the future.

346 The short-term (minute scale) variability of gCH_4 and gCO_2 was apparently influenced by
 347 turbulent mixing with the more dilute atmosphere outside the cave. This was indicated during all
 348 campaigns by rapidly fluctuating gCH_4 and gCO_2 mole fractions (Figure 2a-c) and increasing air
 349 temperature and decreasing humidity of the subglacial air (Figure S3). However, for most of the
 350 time, the relative humidity in the cave remained at 100% and air temperatures were low (below
 351 0.5°C) whereas the outside temperatures were higher (diel variation between $1 - 12^\circ\text{C}$)
 352 indicating an overall low degree of mixing. In particular, the longer-scale diurnal variability is
 353 likely not caused by mixing with the outside atmosphere, but by the subglacial supply of trace
 354 gases. This is supported by the fact that in August 2018 the subglacial air temperature varied in a
 355 pattern that corresponded to the diurnal variation in melt water flow, with highest subglacial air
 356 temperatures observed under maximum flow (Figure S3). Whether the higher subglacial air
 357 temperature is caused by heat dissipation from frictional heating of the turbulent meltwater or
 358 higher influx of relatively warmer surface water is unknown. However, we conclude that the
 359 short-term variability of CO_2 and CH_4 mole fractions in the subglacial cave system is a direct
 360 product of occasional turbulent mixing at the interface between the ice cave and the atmosphere,
 361 whereas the diurnal cycle of gCH_4 and gCO_2 and total net emission we observe (Fig. 2A-C) is
 362 directly related to the flow of melt water and not the atmospheric conditions outside the cave.

363 *Table 2 Flux range estimates of CH_4 and CO_2 for the non-water filled cross section of the subglacial river outlet for the May*
 364 *2019, June 2018 and August 2018 campaigns.*

Cross section	Subglacial air	Hourly average	Hourly average
---------------	----------------	----------------	----------------

	area	velocity*	CH ₄ emission**	CO ₂ emission**
Unit	m ²	m s ⁻¹	g CH ₄ h ⁻¹	g CO ₂ h ⁻¹
May 2019	0.30 - 1	0.8	30 – 200	520 – 3620
June 2018	3-4	0.8 ± 0.28	170 – 460	5920 – 16400
August 2018	8 - 10	0.8	200 – 510	14100 – 36610

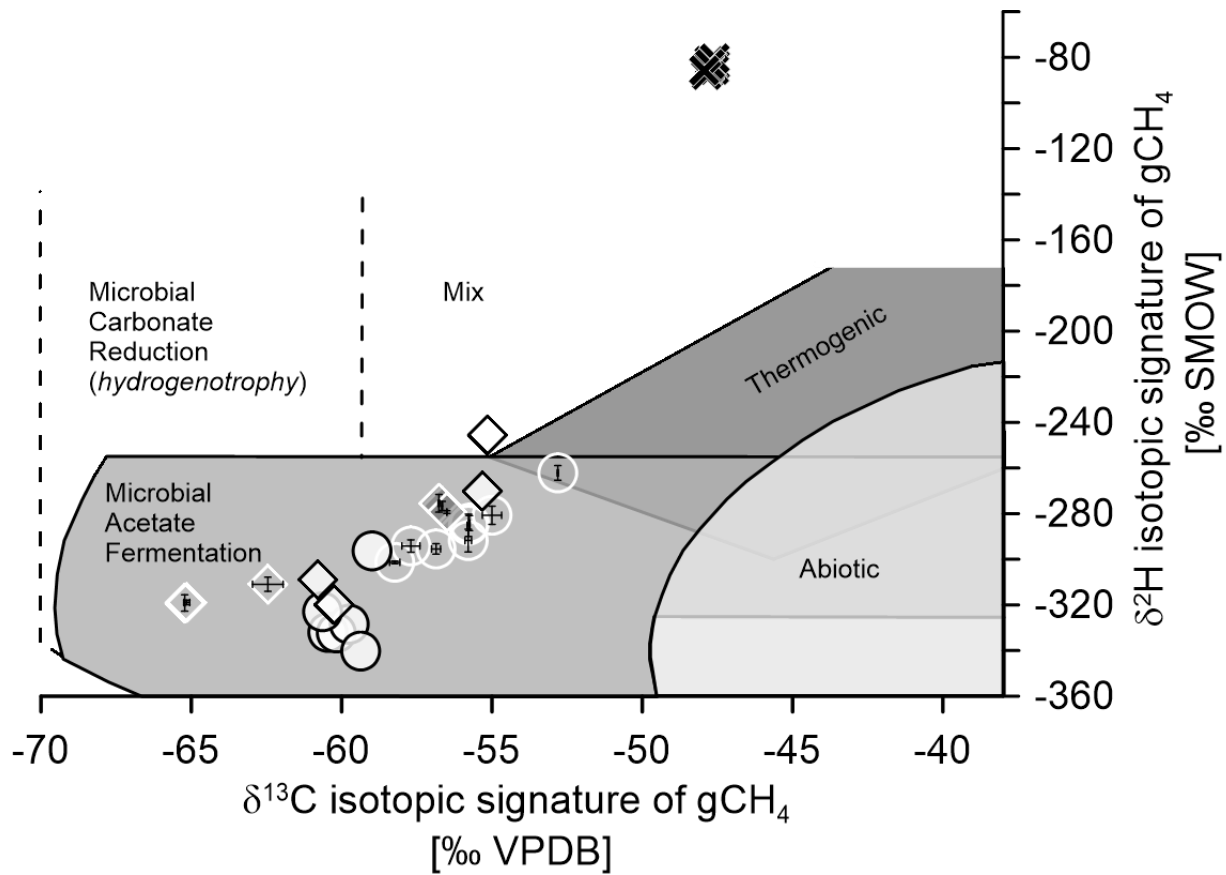
365 *Average±standard deviation of measurements for a three day period in June 2018. Used also for May 2019 and
 366 August 2018, **fluxes are rounded to the nearest 10.

367 3.2 Isotopic composition of subglacial CH₄ and CO₂

368 Figure 3 shows a dual isotope plot of the isotopic signatures ($\delta^{13}\text{C-CH}_4$ and $\delta^2\text{H-CH}_4$)
 369 estimated from separated Keeling plots (Figure S4A-D), for gaseous CH₄ and the isotopic
 370 composition of the dissolved CH₄. compared to measurements of $\delta^{13}\text{C}$ and $\delta^2\text{H}$ values of discrete
 371 gas samples for ambient air. These estimates clearly indicate that dCH₄ and gCH₄ originate from
 372 microbial acetate fermentation.

373 The $\delta^{13}\text{C}$ values of dCH₄ at PW1 were depleted compared to the atmosphere and varied
 374 little during each campaign and between June and August campaigns, suggesting a similar source
 375 over the melt season. The isotopic signature of gCH₄ was slightly enriched in both ¹³C and ²H
 376 and more variable compared to $\delta^{13}\text{C}$ values for dCH₄ for most of the June and August (Figure 3,
 377 Figure S4).

378 The isotopic signatures ($\delta^{13}\text{C}$ and $\delta^2\text{H}$) of gCH₄ varied along a line (slopes ≈ 5 and 7.4
 379 for June and August 2018 campaigns, respectively) that resembles an oxidation pattern (Figure
 380 3) suggesting *in situ* transformation of the subglacial CH₄. This points to the presence of an
 381 active biological system below the ice, but its importance for modifying CH₄ emission to the
 382 atmosphere is still unknown. The slope is smaller than what has earlier been attributed to
 383 oxidation of dCH₄ ($\alpha=8.6-9$) (Burns et al., 2018; Etiope & Sherwood Lollar, 2013) and while this
 384 indicates that oxidation of subglacial CH₄ takes place, the lower slope for gCH₄ we find suggests
 385 additional isotope fractionation processes could impact the isotopic signature of gCH₄. Future
 386 research will focus on understanding what drives the deviation between the isotopic signature of
 387 gCH₄ and dCH₄ as it has implications for interpretation of the origin of subglacial CH₄.



388
 389 **Figure 3** Dual isotope plot of Keeling plot estimates of the isotope source signatures ($\delta^{13}\text{C-CH}_4$ and $\delta^2\text{H-CH}_4$) for
 390 gCH_4 (transparent symbols and white marker line) in June 2018 (circles) and August 2018 (diamonds). Standard
 391 errors of the estimate of isotopic signature (gCH_4) are shown as error bars. Isotopic composition ($\delta^{13}\text{C-CH}_4$ and $\delta^2\text{H-}$
 392 CH_4) of dCH_4 are shown in white symbols with black edge for June 2018 (circles) and August 2018 (diamonds)
 393 campaigns. Grey shaded areas modified after Whiticar (1999). For comparison, the $\delta^{13}\text{C}$ and $\delta^2\text{H}$ values of
 394 atmospheric CH_4 are shown with X's.

395 Further evidence of an active microbial transformation of the subglacial CH_4 and CO_2
 396 emissions is provided by the relation between isotopic $\delta^{13}\text{C}$ signatures of dissolved and gaseous
 397 subglacial CH_4 and of gaseous subglacial CO_2 (Figure 4a & b). The difference (-6 to 22‰)
 398 between the $\delta^{13}\text{C}$ isotopic signatures of gCO_2 and gCH_4 , suggests that a substantial proportion of
 399 the subglacial gCO_2 is derived from CH_4 oxidation in the subglacial environment (Whiticar,
 400 1999). Using the Keeling plot approach for $\delta^{13}\text{C}$ of gCO_2 (Figure S5) shows that the samples
 401 group in the zone of CH_4 oxidation on the dual isotope plot (Figure 4b). This provides field
 402 experimental confirmation for subglacial CH_4 oxidation to CO_2 which in previous studies has
 403 only been inferred indirectly (Burns et al., 2018).

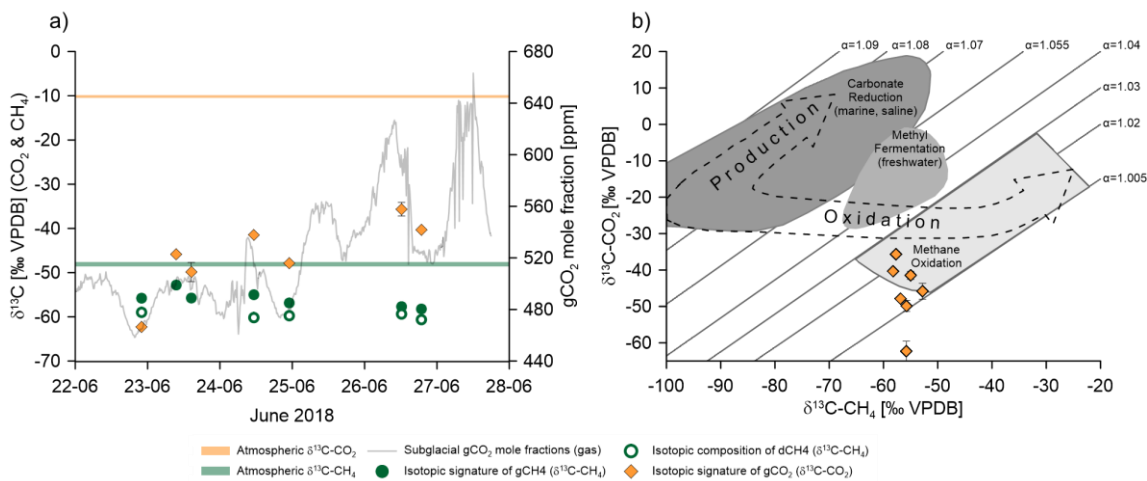
404 We also observed that less $\delta^{13}\text{C}$ -depleted gCO_2 corresponded to increasing gCO_2 mole
405 fractions (Figure 4a). This cannot be explained by the subglacial CO_2 originating only from CH_4
406 oxidation, which produces ^{13}C -depleted CO_2 and indicates that one or more additional and
407 isotopically heavier sources of CO_2 contribute to subglacial CO_2 . Mixing of subglacial air with
408 isotopically heavier atmospheric CO_2 could in principle enrich the gCO_2 in ^{13}C (as we observed
409 for $\delta^{13}\text{C}\text{-CH}_4$), but it cannot increase gCO_2 mole fractions above the ambient level (Figure 2a-c).

410 Instead, it is possible that the increasing mole fraction and ^{13}C -enrichment of gCO_2 could
411 be due to an increased proportion of gCO_2 (and dCO_2) originating from remineralized subglacial
412 organic carbon (Pain et al. 2020), as the export of dCO_2 from remineralization of organic carbon
413 in subglacial sediments must also be governed by melt flow and subsequent degassing into the
414 subglacial air. Subglacial dissolved organic carbon at this outlet (Andrews et al., 2018), a
415 possible substrate for both methanogenesis and remineralisation, was much more enriched ($\delta^{13}\text{C}\text{-}$
416 DOC : -29.8 to -24‰) in ^{13}C than subglacial CH_4 . Subglacial CO_2 that is originating from this
417 carbon pool should therefore have a higher $\delta^{13}\text{C}$ isotopic signature than the strongly ^{13}C -depleted
418 CO_2 originating from subglacial CH_4 oxidation.

419 We observed increasing CO_2/CH_4 ratios in the subglacial air from average values
420 between 5 and 10 in May 2019 to average values >80 in August 2018 (Figure S6). This shows
421 that the export and emission of CO_2 changes during the melt season relative to CH_4 (Figure 2a-c,
422 Table 2), which could be driven by increased CH_4 oxidation and/or remineralisation of organic
423 carbon. As the internal drainage system develops until maximum flow over the melt season, the
424 residence time of the subglacial melt water should increase when the melting decreases later in
425 the year. This longer residence time could enhance subglacial CH_4 oxidation and its contribution
426 to dCO_2 , and limit the export and subsequent emission of subglacial CH_4 to the atmosphere.
427 Also, the expanding ablation zone over the melt season connects pockets of subglacial sediment
428 which could not only lead to increased mobilization of CH_4 (Lamarche-Gagnon et al., 2019) (and
429 hence oxidation), but also of remineralization of organic carbon to CO_2 (Kellerman et al., 2020;
430 Kohler et al., 2017). Oxygen availability in the anoxic subglacial environment limits both the
431 oxidation of subglacial CH_4 (Michaud et al., 2017) and remineralization. However, it is plausible
432 that oxygen is supplied to subglacial environments, both from melting of O_2 -containing basal ice
433 or import of oxygenated surface melt water. We observed that the subglacial melt water at the
434 outlet was fully oxygenated to nearly 100% of the atmospheric equilibrium during the June 2018

435 campaign (data not shown) indicating conditions conducive for both processes to occur in the
 436 subglacial environment at this site. An additional possible source of subglacial CO₂ could be
 437 inorganic carbonate dissolution from the bedrock and the size of this contribution is determined
 438 by the endogenous carbonate content of the bedrock and subglacial weathering rates.

439 Thus, several CO₂ generating processes likely occur simultaneously, and how they
 440 contribute to the resulting net emission in the proglacial zone is closely connected to the glacial
 441 hydrology and basal distribution of carbon containing sediment and bedrock of the catchment.
 442 The interaction between these factors complicates the interpretation of δ¹³C-CO₂ values and
 443 future research should focus on partitioning the subglacial CO₂ sources (oxidation,
 444 remineralization, dilution with atmospheric air, inorganic carbon from carbonate dissolution)
 445 using both gCO₂ and dCO₂ together with measurements of subglacial CH₄. This source
 446 identification should enable us to narrow in on where in the subglacial system, in transit with the
 447 meltwater (Dieser et al., 2014; Lamarche-Gagnon et al., 2019) or at the ice-sediment interface at
 448 the subglacial source (Burns et al., 2018; Michaud et al., 2017) the production and release of CO₂
 449 happens.



450
 451 **Figure 4** a) Temporal variation of isotopic ($\delta^{13}\text{C}$) source signatures for gaseous CO₂ (◆) and CH₄ (●) and the isotopic
 452 composition of dissolved subglacial CH₄ (○). Subglacial gaseous CO₂ mole fractions (ppm) are superimposed as grey line.
 453 Vertical error bars for gCO₂ and gCH₄ indicate the standard error of the Keeling plot intercept; in most cases error bars were
 454 smaller than the symbols. indicate the δ¹³C values of atmospheric CO₂ (orange) and CH₄ (green), respectively and b) Dual
 455 isotope plots showing the resulting Keeling plot isotope signature of gCO₂ (δ¹³C-CO₂) plotted against the isotopic signature of
 456 gCH₄ (orange diamonds). Standard errors of the Keeling plot intercept are shown as vertical and horizontal error bars. In most
 457 cases error bars were smaller than the symbols.

458

459 **4 Conclusions**

460 In this study we present direct continuous measurements of gaseous evasion of CH₄ and
461 CO₂ from below the Greenland Ice sheet at three different stages of a melt season. These unique
462 seasonal measurements are supported by isotopic studies of both subglacial CH₄ and CO₂ in
463 discrete gas and water samples and show high emissions of CH₄ and CO₂ from the subglacial
464 environment to the atmosphere. Results show that degassing of dissolved gases happens both
465 under the ice in the subglacial cave system and in the proglacial river system confined to a
466 relatively narrow zone from the outlet.

467 Gaseous CH₄ and CO₂ emissions are closely linked to the glacial hydrology and
468 emissions from the outlet increase over the melt season related to the discharge and development
469 of the subglacial drainage system, allowing more degassing in the subglacial system later in the
470 season. The large emissions of CH₄ and CO₂ point to a significant contribution to the
471 atmosphere. Considering that the phenomenon should also occur at other glaciers along the
472 margin of GrIS and in Iceland, warrants intensified research.

473 The isotopic signatures show that subglacial CH₄ originates from biological production of
474 CH₄ by acetoclastic methanogenesis, likely from buried organic carbon, which is the source
475 throughout the melt season. Isotopic analysis also shows that the emitted subglacial CO₂ is
476 linked to oxidation of this subglacial CH₄. However, the isotopic composition of subglacial CO₂
477 point to other possible sources of subglacial CO₂ apart from CH₄ oxidation and we suggest that
478 remineralisation of organic carbon also contributes to the emission of CO₂ at the outlet. The
479 proportion of CO₂ emission relative to CH₄ increases over the melt season possibly reflects
480 increased oxidation of CH₄ and remineralisation of organic carbon. This is likely fueled by a
481 combination of increased oxygen input from surface water and longer residence time of melt
482 water in the subglacial drainage system. However, it is still unknown where in the subglacial
483 system (sediment, melt water or both) the CH₄ oxidation takes place. The interpretation of the
484 isotope signals suggests that the emitted CH₄ and CO₂ undergo biogeochemical transformation
485 below the ice and that mixing or dilution with other sources during transport under the ice can
486 occur.

487 Our study shows that large amounts of biogenic CH₄ and CO₂ are emitted from the GrIS
488 via glacial meltwater. However, considerable uncertainty still exists, related to the quantification
489 of the exact mass flux of CH₄ and CO₂ due to an unknown partitioning between aqueous and

490 gaseous fluxes, as well as uncertainty of the measurement of physical parameters (e.g. wind
491 speed and direction) controlling the net emission. There is a need to advance the fundamental
492 knowledge of the emission of subglacial CO₂ and CH₄ and the biogeochemical processes
493 governing the production and turnover of subglacial carbon to understand this unknown carbon-
494 cryosphere feedback from glaciers and ice sheets worldwide and determine its importance for the
495 atmospheric composition of CH₄ and CO₂.

496 **Data Availability Statement**

497 The data used in this study has been published and can be accessed online through University of
498 Copenhagens Electronic Research Data Archive (ERDA) (at
499 <https://doi.org/10.17894/ucph.597b96ab-eef5-4be4-b4dd-b21998e2ed3b>)

500 **Acknowledgments**

501 This study was kindly funded by Hartmann Fonden (grant no. A32524). The authors declare no
502 financial conflicts of interests.

503 **References**

- 504 Andrews, M. G., Jacobson, A. D., Osburn, M. R., & Flynn, T. M. (2018). Dissolved Carbon
505 Dynamics in Meltwaters From the Russell Glacier, Greenland Ice Sheet. *Journal of*
506 *Geophysical Research: Biogeosciences*, 123(9), 2922–2940.
507 <https://doi.org/10.1029/2018JG004458>
- 508 Brass, M., & Röeckmann, T. (2010). Continuous-flow isotope ratio mass spectrometry method
509 for carbon and hydrogen isotope measurements on atmospheric methane. *Atmospheric*
510 *Measurement Techniques*. <https://doi.org/10.5194/amt-3-1707-2010>
- 511 Burns, R., Wynn, P. M., Barker, P., McNamara, N., Oakley, S., Ostle, N., et al. (2018). Direct
512 isotopic evidence of biogenic methane production and efflux from beneath a temperate
513 glacier. *Scientific Reports*, 8(1), 17118. <https://doi.org/10.1038/s41598-018-35253-2>
- 514 Christiansen, J. R., & Jørgensen, C. J. (2018). First observation of direct methane emission to the
515 atmosphere from the subglacial domain of the Greenland Ice Sheet. *Scientific Reports*, 8(1),
516 16623. <https://doi.org/10.1038/s41598-018-35054-7>
- 517 Christner, B. C., Montross, G. G., & Priscu, J. C. (2012). Dissolved gases in frozen basal water
518 from the NGRIP borehole: Implications for biogeochemical processes beneath the
519 Greenland Ice Sheet. *Polar Biology*, 35(11), 1735–1741. <https://doi.org/10.1007/s00300-012-1198-z>
- 521 Dieser, M., Broensen, E. L. J. E., Cameron, K. a, King, G. M., Achberger, A., Choquette, K., et
522 al. (2014). Molecular and biogeochemical evidence for methane cycling beneath the
523 western margin of the Greenland Ice Sheet. *The ISME Journal*, 8(11), 2305–16.

- 524 <https://doi.org/10.1038/ismej.2014.59>
- 525 Drake, H., Suksi, J., Tullborg, E. L., & Lahaye, Y. (2017). Quaternary redox transitions in deep
526 crystalline rock fractures at the western margin of the Greenland ice sheet. *Applied*
527 *Geochemistry*, 76, 196–209. <https://doi.org/10.1016/j.apgeochem.2016.12.001>
- 528 Etiope, G., & Sherwood Lollar, B. (2013). Abiotic methane on earth. *Reviews of Geophysics*.
529 <https://doi.org/10.1002/rog.20011>
- 530 Graly, J. A., Humphrey, N. F., Landowski, C. M., & Harper, J. T. (2014). Chemical weathering
531 under the Greenland Ice Sheet. *Geology*, 42(6), 551–554. <https://doi.org/10.1130/G35370.1>
- 532 Hamilton, T. L., Peters, J. W., Skidmore, M. L., & Boyd, E. S. (2013). Molecular evidence for an
533 active endogenous microbiome beneath glacial ice. *The ISME Journal*, 7(7), 1402–12.
534 <https://doi.org/10.1038/ismej.2013.31>
- 535 Jacques, C., Gkritzalis, T., Tison, J.-L., Hartley, T., van der Veen, C., Röckmann, T., et al.
536 (2020). Carbon and Hydrogen Isotope Signatures of Dissolved Methane in the Scheldt
537 Estuary. *Estuaries and Coasts*. <https://doi.org/10.1007/s12237-020-00768-3>
- 538 Kellerman, A. M., Hawkings, J. R., Wadham, J. L., Kohler, T. J., Stibal, M., Grater, E., et al.
539 (2020). Glacier outflow dissolved organic matter as a window into seasonally changing
540 carbon sources: Leverett Glacier, Greenland. *Journal of Geophysical Research:*
541 *Biogeosciences*, 1–16. <https://doi.org/10.1029/2019jg005161>
- 542 Kohler, T. J., Žárský, J. D., Yde, J. C., Lamarche-Gagnon, G., Hawkings, J. R., Tedstone, A. J.,
543 et al. (2017). Carbon dating reveals a seasonal progression in the source of particulate
544 organic carbon exported from the Greenland Ice Sheet. *Geophysical Research Letters*,
545 44(12), 6209–6217. <https://doi.org/10.1002/2017GL073219>
- 546 Lamarche-Gagnon, G., Wadham, J. L., Sherwood Lollar, B., Arndt, S., Fietzek, P., Beaton, A.
547 D., et al. (2019). Greenland melt drives continuous export of methane from the ice-sheet
548 bed. *Nature*, 565(7737), 73–77. <https://doi.org/10.1038/s41586-018-0800-0>
- 549 Magen, C., Lapham, L. L., Pohlman, J. W., Marshall, K., Bosman, S., Casso, M., & Chanton, J.
550 P. (2014). A simple headspace equilibration method for measuring dissolved methane.
551 *Limnology and Oceanography: Methods*, 12(9), 637–650.
552 <https://doi.org/10.4319/lom.2014.12.637>
- 553 Michaud, A. B., Dore, J. E., Achberger, A. M., Christner, B. C., Mitchell, A. C., Skidmore, M.
554 L., et al. (2017). Microbial oxidation as a methane sink beneath the West Antarctic Ice
555 Sheet. *Nature Geoscience*, 10(8), 582–586. <https://doi.org/10.1038/ngeo2992>
- 556 Naus, S., Röckmann, T., & Popa, M. E. (2018). The isotopic composition of CO in vehicle
557 exhaust. *Atmospheric Environment*, 177, 132–142.
558 <https://doi.org/10.1016/j.atmosenv.2018.01.015>
- 559 Pain, A. J., Martin, J. B., Martin, E. E., & Rahman, S. (2020). Heterogenous CO₂ and CH₄
560 content of glacial meltwater of the Greenland Ice Sheet and implications for subglacial
561 carbon processes. *The Cryosphere*, (July), 1–33. <https://doi.org/10.5194/tc-2020-155>
- 562 Pataki, D. E., Ehleringer, J. R., Flanagan, L. B., Yakir, D., Bowling, D. R., Still, C. J., et al.

- 563 (2003). The application and interpretation of Keeling plots in terrestrial carbon cycle
564 research. *Global Biogeochemical Cycles*, 17(1). <https://doi.org/10.1029/2001GB001850>
- 565 Pathirana, S. L., van der Veen, C., Popa, M. E., & Röckmann, T. (2015). An analytical system
566 for stable isotope analysis on carbon monoxide using continuous-flow isotope-ratio mass
567 spectrometry. *Atmospheric Measurement Techniques*, 8(12), 5315–5324.
568 <https://doi.org/10.5194/amt-8-5315-2015>
- 569 Röckmann, T., Eyer, S., van der Veen, C., Popa, M. E., Tuzson, B., Monteil, G., et al. (2016). In
570 situ observations of the isotopic composition of methane at the Cabauw tall tower site.
571 *Atmospheric Chemistry and Physics*, 16(16), 10469–10487. [https://doi.org/10.5194/acp-16-](https://doi.org/10.5194/acp-16-10469-2016)
572 [10469-2016](https://doi.org/10.5194/acp-16-10469-2016)
- 573 Sapart, C. J., van der Veen, C., Vigano, I., Brass, M., van de Wal, R. S. W., Bock, M., et al.
574 (2011). Simultaneous stable isotope analysis of methane and nitrous oxide on ice core
575 samples. *Atmospheric Measurement Techniques*, 4(12), 2607–2618.
576 <https://doi.org/10.5194/amt-4-2607-2011>
- 577 Souchez, R., Lemmens, M., & Chappellaz, J. (1995). Flow-induced mixing in the GRIP basal ice
578 deduced from the CO₂ and CH₄ records. *Geophysical Research Letters*, 22(1), 41–44.
579 <https://doi.org/10.1029/94GL02863>
- 580 Stibal, M., Wadham, J. L., Lis, G. P., Telling, J., Pancost, R. D., Dubnick, A., et al. (2012).
581 Methanogenic potential of Arctic and Antarctic subglacial environments with contrasting
582 organic carbon sources. *Global Change Biology*, 18(11), 3332–3345.
583 <https://doi.org/10.1111/j.1365-2486.2012.02763.x>
- 584 Wadham, J. L., Tranter, M., Tulaczyk, S., & Sharp, M. (2008). Subglacial methanogenesis: A
585 potential climatic amplifier? *Global Biogeochemical Cycles*, 22(2), n/a-n/a.
586 <https://doi.org/10.1029/2007GB002951>
- 587 Wadham, J. L., Arndt, S., Tulaczyk, S., Stibal, M., Tranter, M., Telling, J., et al. (2012).
588 Potential methane reservoirs beneath Antarctica. *Nature*, 488(7413), 633–637.
589 <https://doi.org/10.1038/nature11374>
- 590 Wadham, J. L., Hawkings, J. R., Tarasov, L., Gregoire, L. J., Spencer, R. G. M., Gutjahr, M., et
591 al. (2019). Ice sheets matter for the global carbon cycle. *Nature Communications*, 10(1),
592 3567. <https://doi.org/10.1038/s41467-019-11394-4>
- 593 Whiticar, M. J. (1999). Carbon and hydrogen isotope systematics of bacterial formation and
594 oxidation of methane. *Chem. Geol.*, 161(1–3), 291–314. [https://doi.org/10.1016/S0009-](https://doi.org/10.1016/S0009-2541(99)00092-3)
595 [2541\(99\)00092-3](https://doi.org/10.1016/S0009-2541(99)00092-3)
- 596 Yamamoto, S., Alcauskas, J. B., & Crozier, T. E. (1976). Solubility of methane in distilled water
597 and seawater. *Journal of Chemical & Engineering Data*, 21(1), 78–80.
598 <https://doi.org/10.1021/jc60068a029>

599 **Captions**

600 **Figure 5** Top panel: Map of West Greenland and Isunnguata glacier with study site indicated at
601 red squares (top left inset) and an overview of the study site at the ice front in June 2018. Letters

602 (a, b, c) indicate location of measurement of mole fractions of CH₄ and CO₂ in subglacial air and
 603 sampling of melt water at three different stages during the melt season. a) May 2019 represents
 604 the early stage meltwater discharge where the meltwater openings are small and mostly filled
 605 with water. b) June 2018 represents a progressive stage of opening where multiple cracks and
 606 caves are air filled after the meltwater has carved out channels in the ice. c) August 2018
 607 represents the mature stage of evolution of the meltwater channel, where the volume of the outlet
 608 is at its maximum and most of it is air filled due to decreasing meltwater volumes.

609 **Figure 6** Upper panels (a-c): Time series of gaseous mole fractions of CH₄ (green) and CO₂
 610 (grey) in a) June 2018, b) August 2018 and c) May 2019. Black dashed line indicates the
 611 atmospheric mole fractions of CH₄ (2 ppm) and CO₂ (400 ppm) measured on site. Lower panels
 612 (d-f): Dissolved CH₄ concentrations at three distances (● PW1: 0 m from outlet; ◆ PW2: 200 m
 613 from the outlet; ▲ PW3: 2000 meter from the outlet) for d) June 2018, e) August 2018 and f)
 614 May 2019. Black dashed line indicates the estimated dissolved concentration of CH₄ at
 615 atmospheric equilibrium (0.02 μmol L⁻¹).

616 **Figure 7** Dual isotope plot of Keeling plot estimates of the isotope source signatures (δ¹³C-CH₄
 617 and δ²H-CH₄) for gCH₄ (transparent symbols and white marker line) in June 2018 (circles) and
 618 August 2018 (diamonds). Standard errors of the estimate of isotopic signature (gCH₄) are shown
 619 as error bars. Isotopic composition (δ¹³C-CH₄ and δ²H-CH₄) of dCH₄ are shown in white
 620 symbols with black edge for June 2018 (circles) and August 2018 (diamonds) campaigns. Grey
 621 shaded areas modified after Whiticar (1999). For comparison to the isotopic composition of
 622 dCH₄ and signature of gCH₄ the δ¹³C and δ²H values of atmospheric CH₄ are shown with X's.

623 **Figure 8** a) Temporal variation of isotopic (δ¹³C) source signatures for gaseous CO₂ (◆) and
 624 CH₄ (●) and the isotopic composition of dissolved subglacial CH₄ (⊙). Subglacial gaseous CO₂
 625 mole fractions (ppm) are superimposed as grey line. Vertical error bars for gCO₂ and gCH₄
 626 indicate the standard error of the Keeling plot intercept; in most cases error bars were smaller
 627 than the symbols. indicate the δ¹³C values of atmospheric CO₂ (orange) and CH₄ (green),
 628 respectively and b) Dual isotope plots showing the resulting Keeling plot isotope signature of
 629 gCO₂ (δ¹³C-CO₂) plotted against the isotopic signature of gCH₄ (orange diamonds). Standard
 630 errors of the Keeling plot intercept are shown as vertical and horizontal error bars. In most cases
 631 error bars were smaller than the symbols.

632 **Table 3** Average, minimum and maximum gaseous subglacial CH₄ and CO₂ mole fractions in
 633 May 2019, June 2018 and August 2018 campaigns. *The enrichment factor (xAtmosphere)
 634 relative to the atmosphere for CH₄ and CO₂ is based on in situ measurements of the atmospheric
 635 molefractions of CH₄ = 2 ppm and CO₂= 400 ppm.

636 **Table 4** Emission range estimates of CH₄ and CO₂ for the non-water filled cross section of the
 637 subglacial river outlet for the May 2019, June 2018 and August 2018 campaigns.

Supporting Information for

Carbon emissions from the edge of the Greenland Ice sheet reveal subglacial processes of methane and carbon dioxide turnover

Jesper Riis Christiansen¹, Thomas Röckmann², Maria Elena Popa², Celia Julia Sapart^{3†}, Christian Juncher Jørgensen⁴

¹Department of Geoscience and Natural Resource Management, University of Copenhagen, Denmark

²Institute for Marine and Atmospheric research Utrecht (IMAU), Utrecht University, Netherlands

³Laboratoire de Glaciologie, Université Libre de Bruxelles, Belgium

⁴Arctic Environment, Aarhus University, Denmark

†Current affiliation: CO₂ Value Europe, Belgium

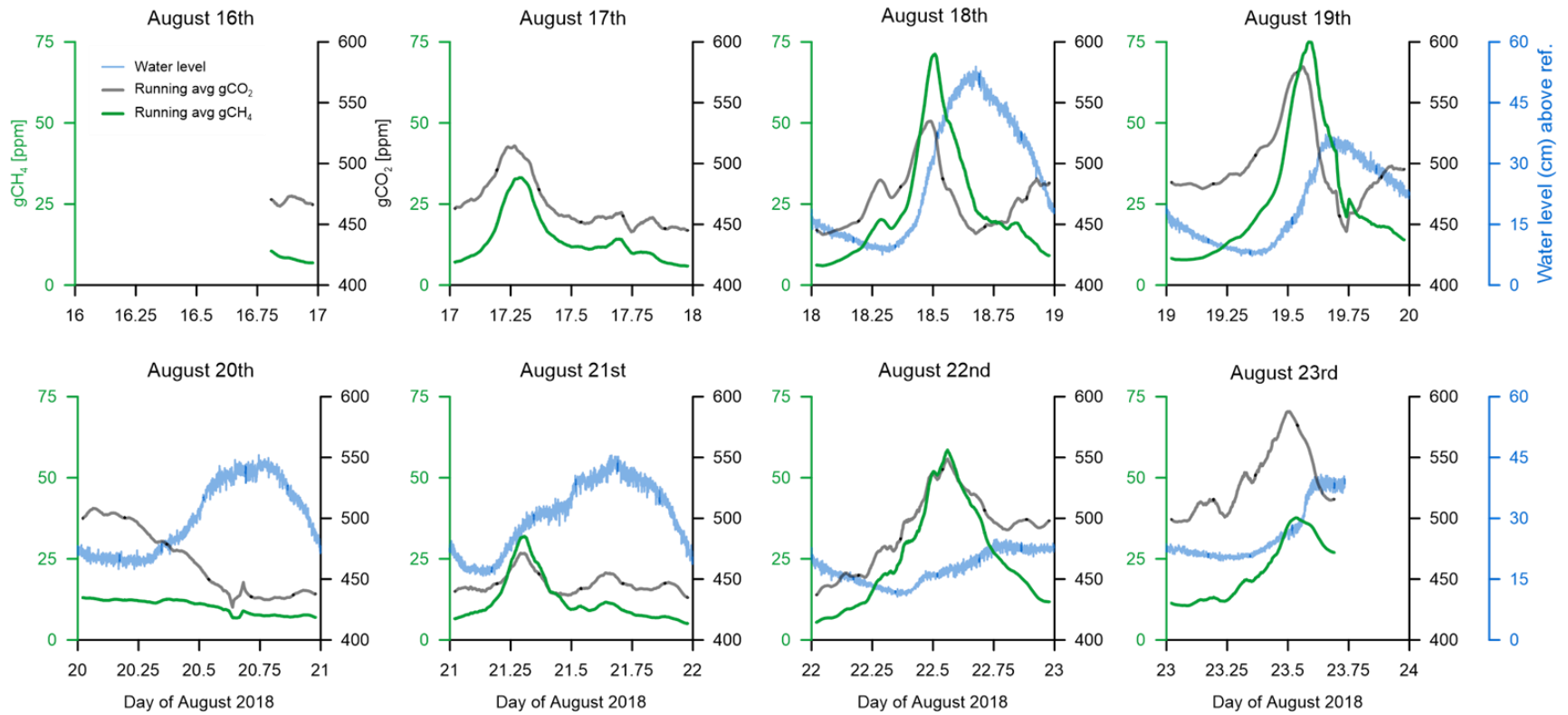
Contents of this file

Supplementary Figures S1 to S6

Introduction

This supplementary material presents additional data on subglacial methane and carbon dioxide mole fractions emitted from the Greenland Ice Sheet as well as their isotopic composition used for determination of the isotopic signature (source) of the subglacial gases. The data presented here was collected over three campaigns during the melting season of 2018 and 2019 representing three typical stages during the melt.

The mole fraction data was measured with a laser spectrometer in the field measuring at 1 Hz the mole fractions of methane, carbon dioxide and water vapor. The isotopic data is based on discrete water and gas samples from the field which were subsequently analyzed in the laboratory.



<Insert Figure S1>

Figure S1. Diurnal variation of gCH₄ (green line), gCO₂ (black line) and water level (blue line) in the outlet river for eight days during the August 2018 campaign. Water level is shown in cm. Time is given as day of the month with decimal hours.

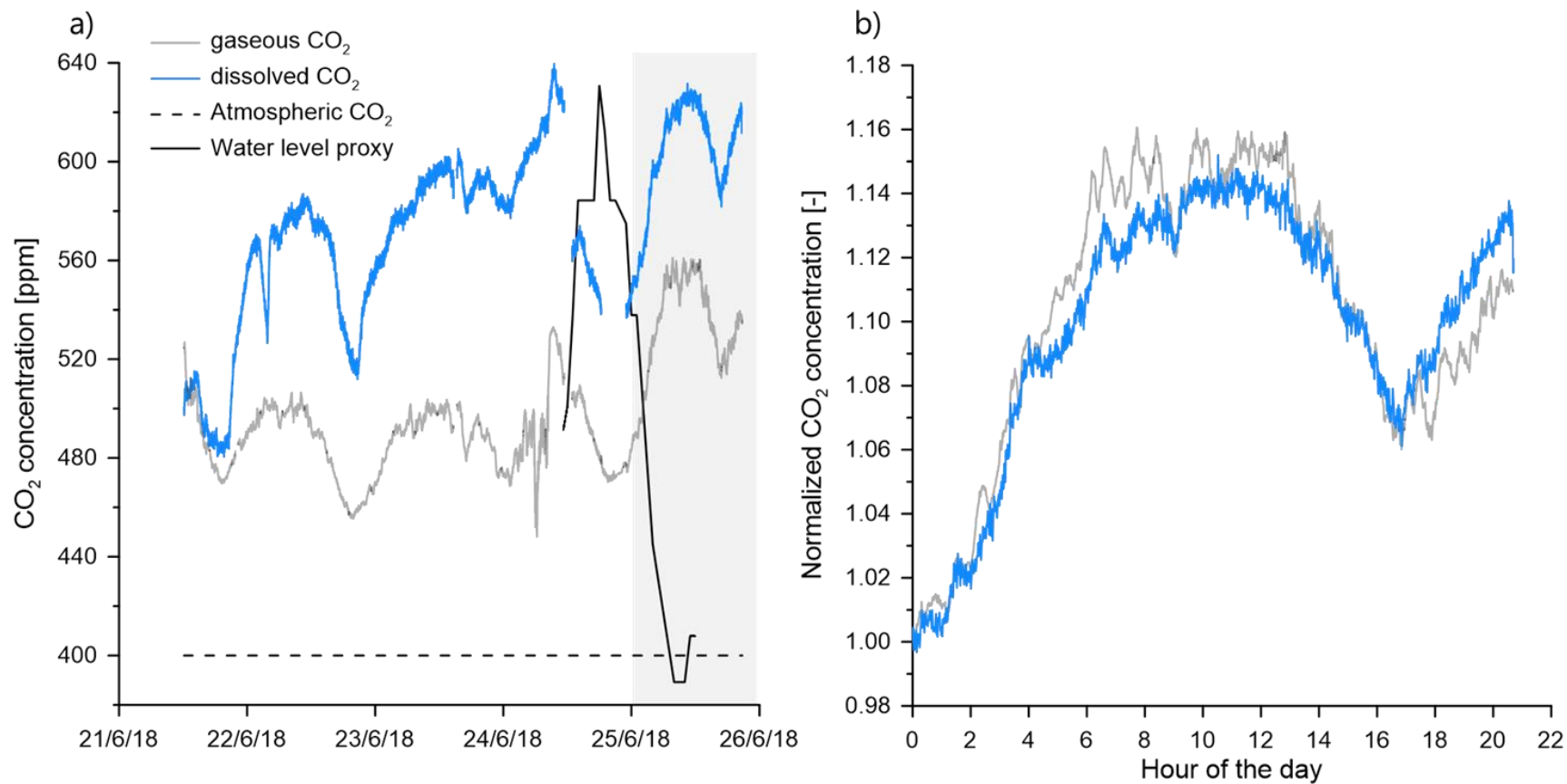


Figure S2 a) Simultaneous measurements of dissolved (blue line) and gaseous (grey line) CO₂ (in ppm) from June 21st to 25th 2019., b) Normalized dissolved CO₂ concentrations and gaseous CO₂ mole fractions for June 25th (shaded area) to elucidate the co-variation of these two fractions. Water level proxy is shown in a black line.

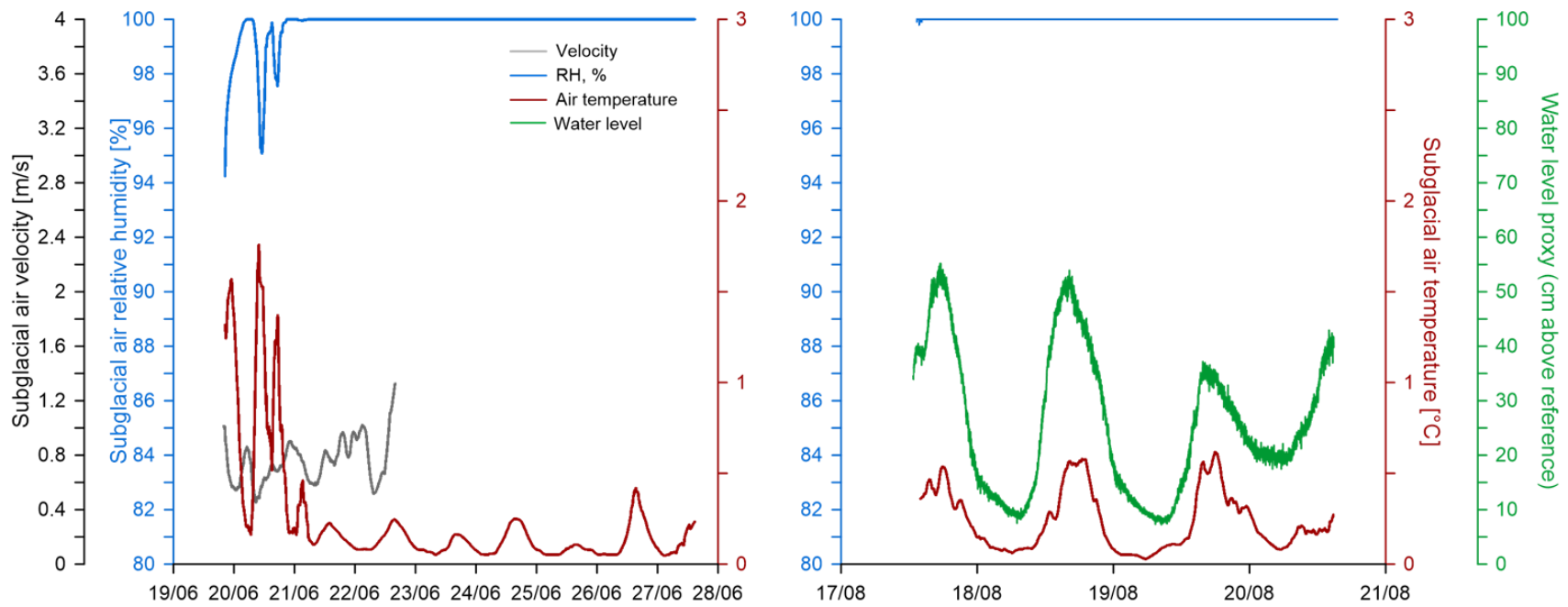


Figure S3 Meteorological parameters measured in the subglacial cavity in June (left panel) and August (right panel): velocity of air (grey), relative humidity (blue) and temperature (red), water level proxy (green). Air velocity was only measured in June and water level proxy was only measured in August. Meteorological variables are given as hourly means.

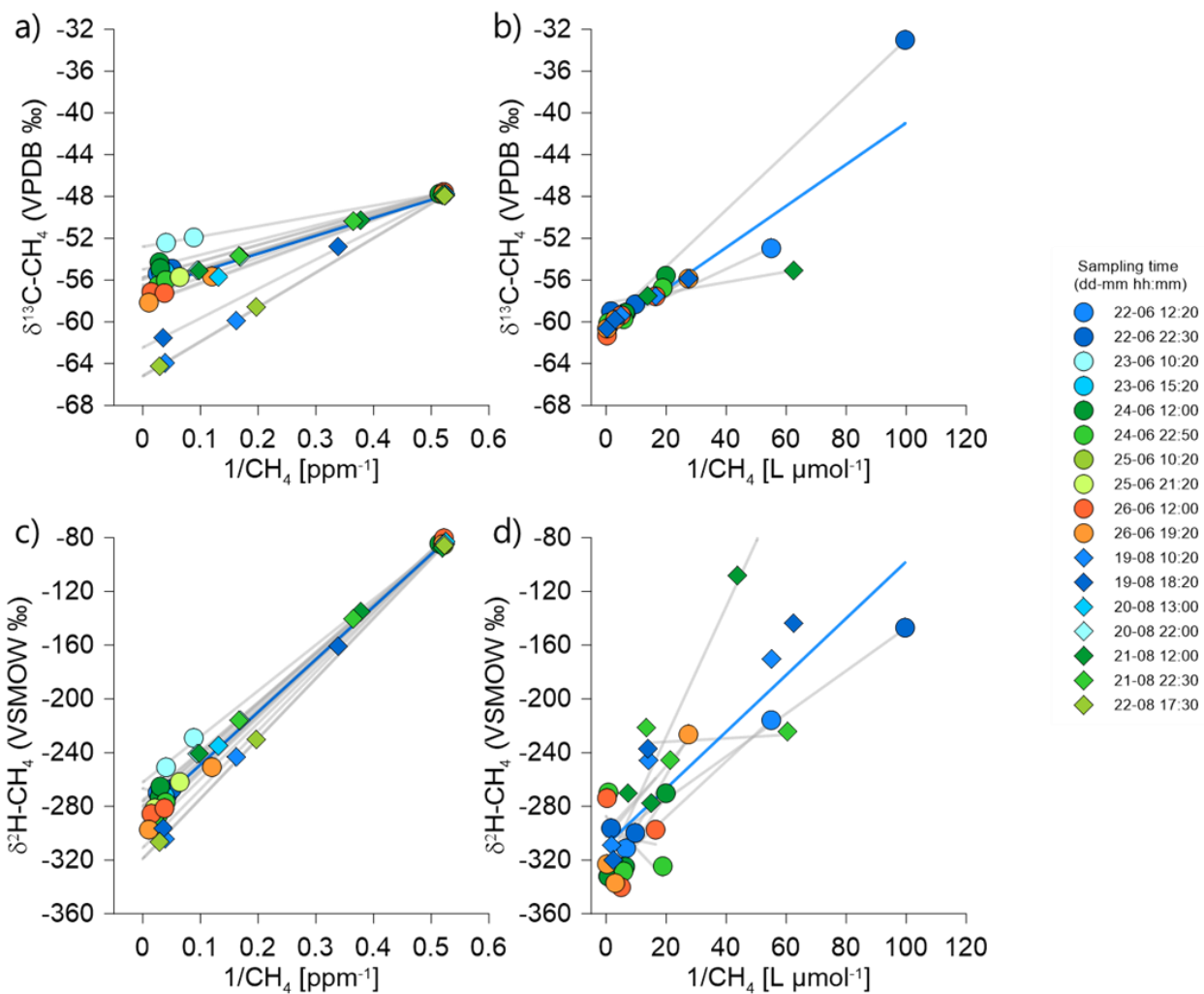


Figure S4 Keeling plots used to determine the isotopic source signature ($\delta^{13}\text{C-CH}_4$ and $\delta^2\text{H-CH}_4$) versus the inverse CH_4 concentration for a) $\delta^{13}\text{C}$ values for gaseous CH_4 , b) $\delta^{13}\text{C}$ values for dissolved CH_4 , c) $\delta^2\text{H}$ values for gaseous CH_4 and d) $\delta^2\text{H}$ values for dissolved CH_4 values for the June (circles) and August (diamonds) 2018 campaigns. The colors represent different sampling times.

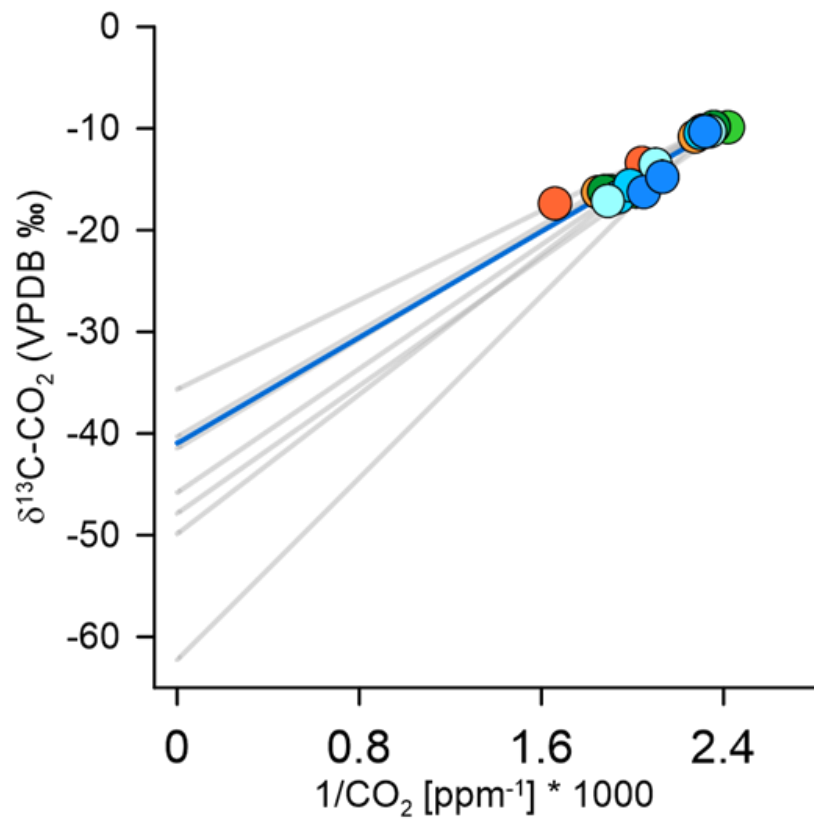


Figure S5 Keeling plots of $\delta^{13}\text{C}$ values of gCO₂. Colors represent different sample dates during the June 2018 campaign (See legend in Supplementary figure 4 for exact times)

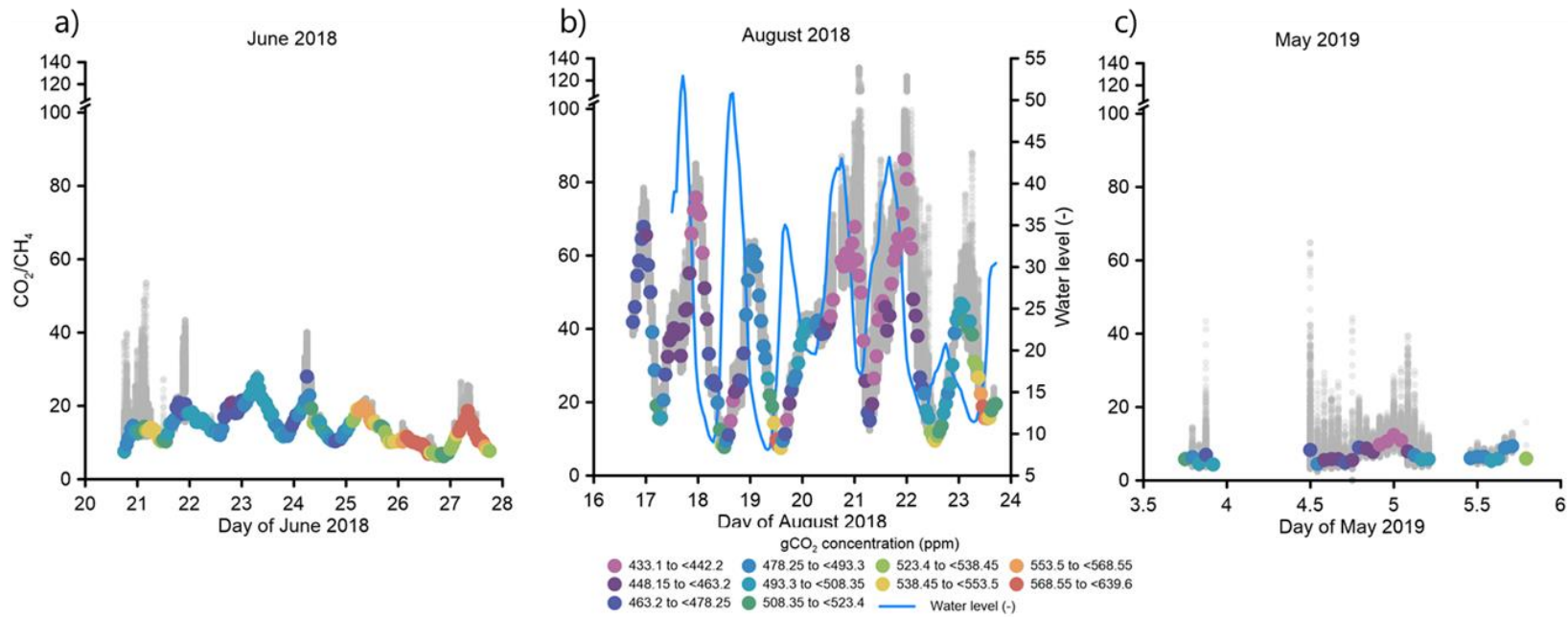


Figure S6 Time series of gCO_2/gCH_4 ratio in subglacial air for a) June 2018, b) August 2018 and c) May 2019. Grey symbols are the gCO_2/gCH_4 at 1 Hz and the colored symbols are hourly averages. The color gradient represents the hourly averaged gCO_2 concentration.